

# Active learning guided design and discovery of thermites with targeted properties

Claudia L. Ramírez,<sup>1</sup> Lea Pillemont,<sup>1</sup> Yasser Sami,<sup>1</sup> Nicolas Richard,<sup>2</sup> Alain Esteve,<sup>1</sup> Matthieu Jonckheere,<sup>1</sup> and Carole Rossi<sup>1</sup>

<sup>1</sup>*LAAS-CNRS, University of Toulouse, France*

<sup>2</sup>*CEA-DAM, Bruyeres le Chatel, France*

(Dated: 29 January 2024)

This paper introduces an active learning-based method designed to guide experiments or computations towards user-defined specific regions, termed "regions of interest," within vast and complex design spaces. The goal is to tailor material properties for specific applications. The practicality and effectiveness of this approach were illustrated through its application to the design of Al/CuO reactive materials, showcasing its utility in two distinct applications: welding and high-energy actuations. In our algorithm, a Gaussian process model (GPR) is constructed on 100 initial data samples. Subsequently, the global optimum is pursued through iterative maximization of an acquisition function. This function aims to achieve a balanced sampling by carefully weighing the trade-off between exploring the unknown areas of the design space (where the standard deviation is highest) and exploiting the regions where favorable outcomes (material properties) are already known (regions of interest). The acquisition function combines three factors linearly with the GPR algorithm: (1) a sigmoid function designed to flatten the highest values while emphasizing small variations, (2) a low-pass filter intended to steer the sampling towards regions of interest, and, (3) an incentive function aimed at promoting exploration in under-sampled areas of the design space. The motivation, rationale and expression of the proposed function are discussed in detail. In addition, we assess the efficiency of our algorithm in guiding the sampling process to rapidly and effectively identify a maximum number of points of interest within 1500 iterations. Results demonstrate the efficiency of this dynamic optimization approach in promptly identifying Al/CuO thermites tailored for welding applications, specifically emphasizing the production of low pressure and high temperature. Additionally, our method demonstrates its capability to discover novel Al/CuO thermite materials optimized for high-energy actuation, with a focus on generating high pressure and temperature. This research clearly represents a significant progress for large-scale problems in material science and engineering, where we desire to predict the effect of feature modification but can only afford a limited number of simulations or experiments due to their very expensive cost.

## I. INTRODUCTION

The influence of data science methods is experiencing rapid growth in materials science<sup>1–4</sup> and proves to be a powerful tool for systematically guide experiments or computations towards specific regions in vast and complex design space. Methods such as Bayesian optimization, classification, genetic algorithms have emerged as a efficient computational paradigm for extracting trends and patterns from large datasets<sup>5–10</sup>. In these approaches, data from both successful and failed experiments are used to train machine learning (ML) models. These models, in turn, predict whether a new data sample (not present in the training set) can exhibit properties superior to those in the training data. However, this improvement comes at the cost of extensive re-training procedures. These methods demonstrate great efficiency when a sufficient number of initial samples are available to train the surrogate. For instance, typical deep neural networks often require a substantial minimal volume of training data, typically ranging between  $10^4$  and  $10^6$  instances (see the interesting discussion<sup>11</sup>). Consequently, these models may not be suitable for case studies involving significantly smaller datasets ( $< 1000$ ).

On the other hand, the discovery and optimization of materials still remains a significant challenge when dealing with a very large feature space (design space), limited data, and, if the experiments and/or calculations are expensive to perform. This is particularly relevant in reactive material design prob-

lems. Reactive materials are mixture of metallic fuel and oxidizer particles of around  $10^2 - 10^4$  nm in size, that undergo an extremely high-temperature combustion (1000 – 6000 K range) and their burn rate and pressurization rate can be tuned in the ranges of  $10^{-1} - 10^4$  m.s<sup>-1</sup> and 1 – 400 MPa.μs<sup>-1</sup>, respectively, by adjusting the metal and oxide particle size, the metal purity, the powder density and the stoichiometry<sup>12–17</sup>. A wide span of additional process and environmental parameters, from pressure, temperatures, to reactants/products species and concentration, can also influence the combustion chemistry and topology, making it extremely difficult to derive one prediction which holds for all conditions. Exhaustive exploration of all these features space, denoted by  $x$ , that characterize the material chemistry, structure, composition, and/or microstructure, to optimize some combustion property denoted by  $y$  is simply experimentally impossible and computationally demanding when using physics-driven models. A standard combustion tests typically performed to characterize the performance of a single reactive material configuration in a one-shot experiment, demands substantial quantities of material (at least tens of milligrams) and necessitates robust and costly safety measures. A few physical models<sup>18–23</sup> do exist but can not be applied for the generation of a large database as requested for ML models.

The focus of this work is therefore to show how calculations from physical models can be guided optimally using active learning<sup>24</sup> to enable the discovery of new Al/CuO reactive materials with targeted properties in as few iterations as

possible to avoid the laborious unguided trial-and-error iterative process. The Al/CuO thermite was selected as the reactive material due to its extensive study and exploration in various applications in civilian and defense applications<sup>25–28</sup>. Additionally, physical models do exist to predict relationships between Al/CuO combustion properties and microstructure data, including the size of metal and oxidizer, purity of metal, and concentrations of reactants, as well as powder compaction<sup>20,23,29,30</sup>.

A key element of our exploration approach involves training a surrogate model to predict material properties while acknowledging the influence of uncertainties arising from statistical inference. This approach enables us to navigate the vast design space for materials, identifying those with superior properties compared to those present in the existing training dataset. Another central idea is that the surrogate model prediction efficiency should be optimized in zones termed "of interest", where material properties are tailored for a particular application, rather than attempting to cover the entire feature space uniformly. As a consequence, we define acquisition functions that strike a balance between uncertainties and predictions from the surrogate model together with a function that prioritizes decision making process in unexplored design spaces. To achieve this, we employ Gaussian process regression<sup>31</sup> (GPR) with customized kernels as surrogates. Within the GPR framework, we then derive acquisition functions through optimization programs. These programs are defined by optimising a tradeoff made of the quantity of interest based on physical inference, an upper confidence bonus and potentially the distance from the previous interesting point in the database.

The contributions provided in this paper are threefold:

- We introduce a active learning strategy using one acquisition function for selecting optimized Al/CuO samples in the vast design space, i.e. a material with properties falling within a specific user-defined range of interest. The acquisition function is formed by combining different factors linearly with a GPR algorithm : 1) a sigmoid function designed to flatten the highest values while emphasizing small variations, 2) a low-pass filter that guides the sampling into a user-defined zone of interest, and, 3) an incentive function that encourages the exploration of under-sampled regions in the design space. The trade-off is only used after a sufficient training of the Gaussian process (between 200 and 300 points).
- We demonstrate that the incentive function for coverage enhances the versatility of the optimization algorithm and enable to discover new thermite materials. This can be particularly useful when the user wants to ensure that the optimization process not only exploits the first found zone of interest but also explores diverse regions of the design space that are totally unknown by the user.
- We demonstrate the efficiency of this dynamic optimization to reach rapidly zones of interest in a vast and unstructured database. Two objectives were explored:

- (1) identify Al/CuO thermites for welding and soldering applications, i.e. giving a combustion temperature and pressure in the range 2000-4500 K and 1 - 2 MPa, respectively.
- (2) Discover new Al/CuO thermite materials for actuation applications requiring very high pressure and temperature, i.e., in the range of 40-56 MPa 5800-7000 K, respectively.

This research represents a huge progress for large-scale problems in material science and engineering, beyond reactive material design, where we desire to predict the effect of feature modification but can only afford a limited number of simulations or experiments due to their very expensive cost.

## II. METHODOLOGY AND COMPUTATIONAL DETAILS

This section provides the notations and basic concepts used all along the paper. We describe the mathematical formulations and give the computational details implemented in the proposed algorithms to efficiently explore the thermite design space,  $\mathbb{X}$ . The typical procedure consists of three major steps (Fig. II D): first,  $m$  Al/CuO thermite configurations (initial dataset) are sampled using the Latin Hypercube Sampling (LHS) to initialize the database (DB). For each sample, the outputs (targets) in terms of maximal combustion temperature ( $T_{max}$ ) and final pressure ( $P_f$ ) are calculated using a physical model and define a given ground true value. Second, an approximation (surrogate) to the merit landscape of the design features is constructed using a GPR process. Third, a new set of features is proposed for the next predictions based on the surrogate, following a sampling strategy defined by an acquisition function, seeking to strike a balance between DB exploration and exploitation as detailed in subsection II D.

### A. Physical model: ground truth values

A physical simulator of the Al/CuO thermite combustion was used to calculate  $T_{max}$  and  $P_f$ , the two targets, as a function of Al and CuO microstructure data. Full details about the model from its physico-chemical foundations and numerical implementation can be found in<sup>23</sup>.

In this current work, we focus on only three design features among a dozen, the Al and CuO particles radius, noted as  $r_{Al}$  and  $r_{CuO}$  respectively, and the Al over CuO molar ratio, or Al richness, noted as  $\phi$ . The range of  $r_{Al}$ ,  $r_{CuO}$  and  $\phi$  values are given in Table ?? corresponding to technological constraints.

### B. Latin Hypercube Sampling

LHS is a systematic and efficient sampling technique dedicated to multiple dimensional problems in statistical studies and simulations. In contrast to uniform random sampling methods, which are susceptible to the concentration of distance effects, LHS ensures a well-distributed representation of values across the design space, offers potentially improved

TABLE I. Description of the features and targets with their range of variation (design space  $\mathbb{X}$ ).

Variables	Description	Range
$r_{Al}$	Aluminum particle radius	0.1 - 10 $\mu\text{m}$
$r_{CuO}$	Copper oxide particle radius	0.1 - 10 $\mu\text{m}$
$\phi$	Aluminum richness	1 - 4
$T_{\max}$	Maximal combustion temperature	600 - 7500 K
$P_f$	Gas pressure	0.2 - 150 MPa

coverage, and, reduces the chances of overlooking parameter areas. In addition to initialization, LHS is employed as a benchmark algorithm to assess all active learning algorithms proposed in this study. To accurately assess the comprehensiveness of the obtained results, we also conducted a LHS study comprising 19404 samples, i.e. the physical simulator was utilized to span the entire range of features as reported in Table I.

### C. Review of Gaussian Process Regression

Gaussian process regression<sup>31</sup> is used to construct the surrogate for the objective function. Briefly, mathematically, we posit that the output  $y$  can be expressed as  $y = g(x) + \varepsilon$ , where  $\varepsilon$  is a Gaussian noise, and  $g : \mathbb{R}^D \rightarrow \mathbb{R}^d$ , with  $D$  the number of features (3 in our case) and  $d$  the outputs (targets) of the model. More precisely, the GPR model assumes a prior distribution over each sample in the design space, represented by a mean function  $\mu(\cdot)$  and a covariance function  $k_\theta(\cdot, \cdot)$ , also called kernel.  $\mu$  represents the value of  $g$ , while the kernel captures the similarity or correlation between input points and thus significantly influences the predictions efficiency<sup>31</sup>. Various types of kernels are used in practice, including the constant, linear, squared exponential (RBF), Matérn, white noise, and more. The package for GPR on Scikit-Learn<sup>32</sup> was employed with the RationalQuadratic kernel and the default values for their parameters, except for the *length\_scale\_bounds*, with a range of  $[10^{-7} - 10^5]$ .

From a learning perspective, GPR is a probabilistic regression model, utilizing a training dataset to approximate the posterior distribution for each target,  $y$ . With the initial set of training samples  $(x_i, y_i)_{1 \leq i \leq m}$ , the goal is to achieve generalization to unknown data by making predictions while estimating the associated uncertainty, quantified through the variance of the GPR at each point. In subsequent discussions, the notation  $FIT_{GP}((x_i, y_i)_{1 \leq i \leq m})$  is employed to represent the optimization step for determining the best weights  $\theta_m$  of the GPR.  $\hat{g}$  denotes the GPR approximation of the function  $g$ . Noteworthy, unlike many other learning algorithms, one of the significant advantages of the GPR is their ability to offer transparent quantifications of uncertainty, achieved through estimates of standard deviations. For constructing the GPR surrogate, we employed the features presented in Table I and considered the  $P_f$  and/or  $T_{\max}$ , as targets  $y$ .

### D. Multistage sampling strategy based on active learning

Active learning is a paradigm within supervised machine learning that optimizes prediction accuracy with a reduced number of training samples. It achieves this by iteratively training a predictor (surrogate) and utilizing the predictor in each iteration to select training examples that contribute the most to accuracy improvement. Numerous recent research endeavors have concentrated on refining acquisition functions for GPR across various application domains, as exemplified by<sup>33,34</sup>.

Thus the optimization results are incrementally improved by interleaving exploration and exploitation steps. We implemented this methodology to ensure a thorough exploration of the design space and avoid getting stuck in local minima, which might limit the discovery of optimal material properties.

The sampling strategy is therefore defined through one acquisition function  $F_{\theta_k}(\cdot)$  seeking to obtain a balanced sampling by considering a trade-off between exploring the *unknown* areas of  $\mathbb{X}$  (where the standard deviation is highest), and exploiting the areas where a good outcome ( $T_{\max}$  and  $P_f$ ) is known (defined as region of interest).

$$F_{\theta_k}(u, t) = E(\sigma_{\theta_k}(u)) + I(\hat{g}_{\theta_k}(u)) + C_\varepsilon(u, (x_i)_{i \leq k}) \quad (1)$$

The function  $E$  was chosen as a sigmoid function in order to flatten the highest values (including outliers) while increasing the importance of small variations:

$$E(\sigma_{\theta_k}(u)) = \exp(-a \cdot \sigma_{\theta_k}(u)) \quad (2)$$

where  $a$  is obtained considering the minimum and maximum values of standard deviations that could be obtained from the initial data set. It is important to note that this function will be extremely sensible to the initial samples, since the hyper-surface that we want to explore has large discontinuities, which could be poorly predicted by the initial surrogate if there is no sample near the discontinuities. The calculation methodology for the initial dataset size ( $m$ ) and parameter  $a$  is provided in the Supplementary Information, sections A and B, respectively.

Considering that standard deviations can be influenced by outliers or unexplored regions outside the intended scope of interest, potentially exerting undue influence on the selection process, we have introduced a function  $I$ , acting as a simple low-pass filter. This addition aims to mitigate the impact of these values in the optimization algorithm, thereby guiding the sampling into the user-defined zone of interest for a more accurate and robust selection process.

Recall that (1)  $\theta_k$  represents the weight parameters obtained from the GPR fitting on the  $k$  previously obtained samples, and (2) the prediction of the GPR for an input  $u$  is denoted by  $\hat{g}^{\theta_k}(u) = (\hat{g}_i^{\theta_k}(u))_{i=1, \dots, d}$ .

$$I(\hat{g}_{\theta_k}(u)) = \prod_{i=1}^d \left( 1 + \frac{1}{1 + \exp(c_1 + D_i(\hat{g}_i^{\theta_k}(u)))} \right) \quad (3)$$

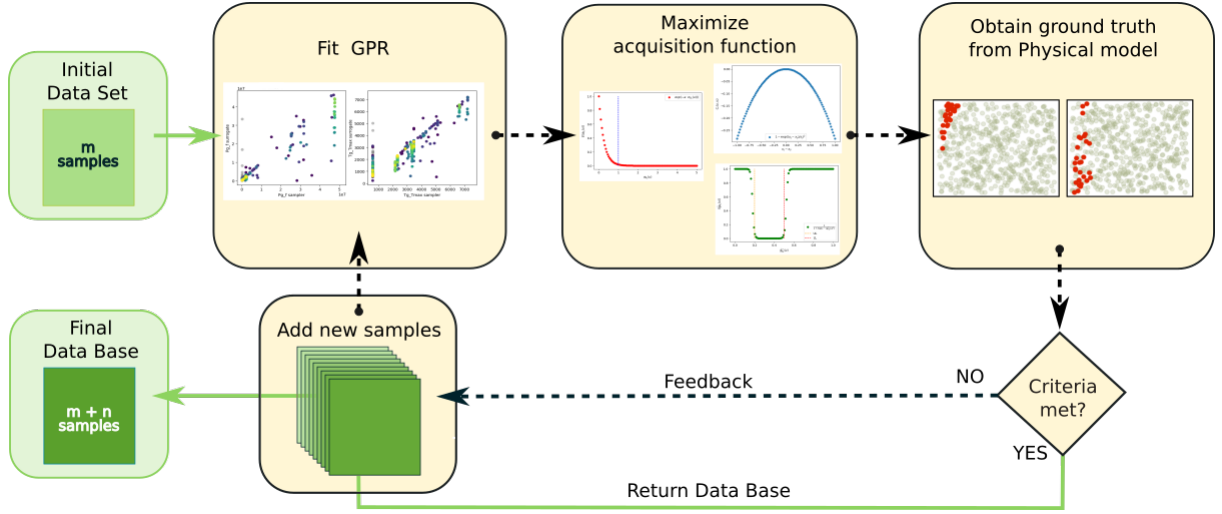


FIG. 1. Schematic of the active learning strategy algorithm. An initial dataset with  $m$  points is built to initiate the training of the surrogate by fitting the GPR. Then, the acquisition function is optimized to obtain a set of sample candidates to explore. The ground truth of each candidate is calculated through the physical model, fitting again the surrogate model to obtain a new predictive distribution. The dotted black line represents the loop responsible for constructing the database, which halts based on criteria such as no improvement or reaching the maximum budget, and then returns the constructed database.

where

$$D_i(s) = c_2(s^2 - L_i)/(U_i - L_i) \quad (4)$$

$d$  defines the dimensional space of the region of interest defined by the users (amount of targets).  $L_i$  and  $U_i$  are the lowest and upper limit of the region of interest in dimension  $i$  respectively.  $c_1$  and  $c_2$  are factors providing the desired filtering.

**CHANGE THOSE VALUES GIVEN THE NEW DEF** We used values of 30 and 10 for  $c_1$  and  $c_2$  respectively.

The term  $C_\epsilon$  is the incentive function for exploration aiming at encouraging the exploration of under-sampled regions in the  $\mathbb{X}$ .

$$C_\epsilon(u, (x_i)_{k < i}) = \frac{e^{-\Gamma^2(u)}}{1 + e^{-\Gamma^2(u)}}, \quad (5)$$

with

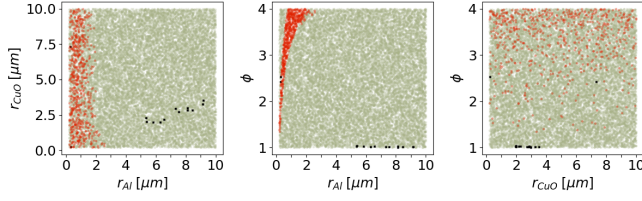
$$\Gamma^2(u) = \sum_{i \in k} \sum_{j \in D} \left( \frac{u_j - (x_i(j))}{\epsilon_j} \right)^2 \quad (6)$$

$(x_i)_k$  are the already explored points and  $\epsilon_j$  is a physical parameter that defines the density information for each feature  $j$  ranging from 1 to 3 as for our study,  $j=3$ .

### E. Active learning workflow and algorithm

We dynamically adjust the acquisition function based on the characteristics of the data and the predictions made by the GPR model. Concretely, the multi-stage sampling strategy can be divided into 4 main steps.

- **Step 1. Preparation of system.** The user specifies a range of interest for the targets ( $T_{\max}$  and  $P_f$ ), which characterize the desired combustion properties for the targeted application. Each thermite that yields the desired combustion properties within the user-defined region is referred to as a point of interest. Next, all variables (Table I) are scaled between 0 and 1, to help the algorithm to achieve better and faster results. The user also enters the coverage parameter  $\epsilon_j$  for each feature  $j$ . The typical range for  $\epsilon_j$  is between 0.2 and 0.5.
- **Step 2. Initial guided sampling with GPR.** We initiate the sampling process by employing GPR to predict the output values (targets) based on the input features:  $r_{Al}$ ,  $r_{CuO}$ , and  $\phi$ . This enables the exploration of points with high standard deviation (STD), leading to a more accurate surrogate.
- **Step 3. Activation of interest term  $I$  of the acquisition function.** When we determine that the surrogate within the region of interest is of satisfactory quality, we activate the interest function  $I$  (which depends on the surrogate's prediction). It is crucial to note that the term  $I$  is deemed to have reached its maximum effectiveness when the sampling within the region of interest decreases, indicating a reduction in proportion over the entire set of samples. This assessment is conducted every 100 new sampled points.
- **Step 4. Activation of coverage term  $C$  of the acquisition function.** When the density of sampled points in the regions of interest within the database is deemed sufficiently high, the incentive function  $C$  of the acquisition function is triggered. This implies that, in addition to considering standard deviation and region of inter-



est, the optimization process incorporates the density of sampled points in specific regions of the input space.

The general algorithm of this sampling strategy is given below.

---

#### Algorithm 1 Active Learning

---

**Require:**  $I_R, (x_i, y_i)_{i \leq m} \in \mathbb{X}$   
**scale**  $\mathbb{X} \rightarrow \mathbb{X}_{[0,1]}$   
**compute**  $\theta_m, \hat{g} \leftarrow FIT_{GP}((x_i, y_i)_{i \leq m})$   
**while**  $t \leq n \mid \delta(x_t \in I_R) \leq \varepsilon$  **do**  
     $x_t \leftarrow MIN[F_{\theta_{t-1}}(u)]_{\{u \in \mathbb{X}_{[0,1]}\}}$   
     $y_t \leftarrow g(x_t)$   
     $\theta_t, \hat{g} \leftarrow FIT_{GP}((x_i, y_i)_{i \leq m+t})$   
**end while**  $\triangleright$  **return**  $(x_i, y_i)_{i \leq m+n}$

---

### III. RESULTS AND DISCUSSION

The developed active learning strategy is analyzed and discussed through the exploration of two distinct applications of Al/CuO thermites. In a first subsection, we evaluate the relative role and efficiency of parts *I* and *C* of the acquisition function to effectively navigate within the design space  $\mathbb{X}$  iteratively and identify Al/CuO thermites giving a combustion temperature and pressure in the range 2000-4500 K and 1 - 2 MPa, respectively. These specified Temperature-Pressure values define the region of interest 1 (referred to as R1) for the exploration. In this specific scenario, the motivation is to design thermite materials that are well-suited for applications related to welding and soldering. In a second subsection, we analyze the relevance and efficiency of the part *I* and *C* of the acquisition function to explore new thermite materials that could not be discovered from human inference. For that second section, we consider applications requiring very high pressure and temperature, i.e., in the range of 40-56 MPa 5800-7000 K, respectively. These specified Temperature-Pressure values define the region of interest 2 (R2).

As a mean to get a reference estimate of both regions 1 and 2, we ran 19404 simulations using the brute force LHS technique. Figure 2 depicts the spatial distribution of the thermites of interest (in red) within the design space  $\mathbb{X}$  corresponding to the region 1 (top) and region 2 (bottom).

The 653 thermites of interest (out of 19404 points) for welding applications (region of interest R1) exhibit specific characteristics. We observe that the aluminum radius is constrained to be below 3  $\mu\text{m}$ , while the copper oxide radius can

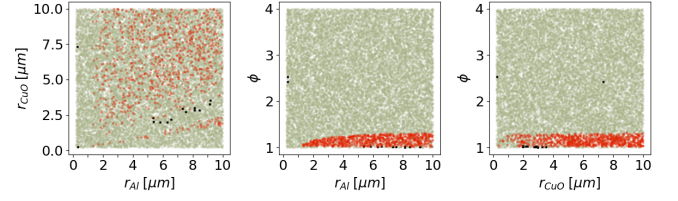


FIG. 2. Spatial distribution of points of interest (red balls) within the design space  $\mathbb{X}$ , obtained employing LHS projected onto main feature scale planes. (Top): region of interest, R1 (653 points of interest); (bottom) region of interest, R2 (988 points of interest). Gray balls represent non-interesting points (18737 points for R1 and 18402 points for R2), and black crosses indicate outliers (out of the range, 14 points). The total number of sampled points is 19404.

span the entire range (100 nm - 10  $\mu\text{m}$ ). The richness falls within the range of 1.2 to 4, with a denser spread of samples as the richness increases. Decreasing the richness requires the aluminum radius to be diminished below 1  $\mu\text{m}$ .

The 988 thermites of interest for actuation applications (Figure 2, bottom) display distinct characteristics. Both the aluminum and oxide radius are microscopic, and the aluminum richness is below 1.5. The primary metric for assessing efficiency will be the ratio of sampled points of interest to the total number of sampled points.

#### A. Region 1 guided exploration: finding Al/CuO thermite materials with low pressure generation for welding application

Herein we will evaluate the efficiency of our algorithm in guiding the sampling process to swiftly and effectively identify the maximum number of points of interest among the 653. The primary metric for assessing efficiency will be the ratio of sampled points of interest to the total number of sampled points.

As a first step, an initial dataset of 100 initial points ( $m$ ) chosen in the design space  $\mathbb{X}$  are used to perform the initial training of the surrogate. As the LHS technique only is used to provide this initial dataset, these first 100 points are uniformly covering the three-dimensional space under consideration for exploration. It is noteworthy that 4% of the 100 points aligns with the Temperature-Pressure region selected as the region of interest R1. Then, we explore the design space by incrementally adding up to 1400 new samples to the database in batches of 100. As a benchmark study, we compare first the non-iterative LHS method, proposing an homogeneous distribution of samples within the explored space, and GPR-only, which provides iterative exploration directions based on the standard deviation from the true function. Table ?? summarizes the number of points of interest (in #) that are sampled when increasing the database by batches of 100 samples. The percentages of points of interest relative to the total sampled points (in %) are highlighted in *italics*.

The LHS method does not show remarkable progression in the number of samples within the region of interest. Starting at 4% of such points after sampling the initial 100 points, the

TABLE II. Evolution of the number of points of interest (in #) and their ratio in % over the total number of sampled points (in italics) calculated after each increment of 100 additional points. It is important to note that LHS as a non iterative procedure is provided for comparison purpose.

Added points	LHS		GPR		GPR+I		GPR+I+C	
	in #	in %	in #	in %	in #	in %	in #	in %
100	6	3	14	4.7	14	7	14	4.7
200	9	3	33	11	33	11	33	11
300	13	3.2	44	11	77	19.2	77	19.2
400	15	3	59	11.8	79	15.8	79	15.8
500	20	3.3	65	10.8	89	14.8	89	14.8
600	26	3.7	69	9.9	131	18.7	131	18.7
700	31	3.9	69	8.6	192	24	192	24
800	37	4.1	69	7.7	235	26.1	257	28.6
900	43	4.3	69	6.9	262	26.2	322	32.2
1000	46	4.2	69	6.3	301	27.4	384	34.9
1100	50	4.2	72	6	343	28.6	444	37
1200	53	4.1	72	5.5	391	30.1	503	38.7
1300	55	3.9	72	5.1	436	31.1	558	39.9
1400	57	3.8	72	4.8	476	31.7	605	40.3

ratio slightly decreases to 3% upon doubling the sampling and then stagnate at around 3 - 4%. This early saturation indicates that no additional specific region of interest emerges from the uniform sampling. This is confirmed from the comparison of the point distribution obtained when sampling the 1500 points (1400 points of Table II + 100 initial points), compared with the LHS benchmark shown in Figure 3. This figure plots the spatial distribution of the 1500 sampled points projected onto the 3 feature scales ( $r_{\text{CuO}}$ ,  $r_{\text{Al}}$  and Al richness) and considers all exploration strategies). At lower levels of sampling, the single cloud of points of interest is well identified and exhibits a similarly homogeneous distribution, albeit with a more limited spatial extension at the cloud borders.

When employing GPR only for guiding the sampling (column "GPR" in Table II), a net enhancement in sampling performance towards points of interest is observed compared to uniform sampling, especially in the initial exploration stages. Adding 200 samples to the database, GPR yields to more than 3 times the saturation percentage obtained with LHS: a plateau is observed with a ratio that stabilizes at approximately 11%, up to the addition of 500 samples. This saturation at  $\sim 11\%$  may be attributed to the thorough exploration of a broad region, leading to a reduction in the standard deviation associated with points in that area. As a result, the exploration can be brought to some other regions of space where the standard deviation will be still high without being located in the region of interest. From this perspective, we observe that beyond 500 samples in the database, the ratio of points of interest continuously diminishes, dropping down to a value of nearly 5%. Therefore, we can conclude that the acquisition function has reached its limit in terms of further exploration. Importantly, the analysis of the points' distribution in Figure 3 provides a clear indication of the limitation of GPR guiding process based on the standard deviation : the distribution of selected points becomes inhomogeneous, revealing clustering or spa-

tial stagnation in specific zones compared to LHS. These clusters include some of the points of interest but are not limited to them.

Activating now  $I$  into the acquisition function after sampling 200 new points with GPR (column "GPR+I" in Table II), we observe a rapid improvement in sampling efficiency towards the region of interest. The number of interest points increases quasi continuously. However, the efficiency of sampling interest points (expressed as a percentage, %) exhibits some erratic behavior at the beginning, specifically for the lines corresponding to 400 and 700 added points. This is attributed to irregularities in the target space ( $P_f$  and  $T_{\text{max}}$ ), especially within the region of interest. As a result, the surrogate may not provide accurate predictions in the early stages. However, after adding 400 more sampled points (line corresponding to 700 added points), we observe a consistent enhancement in the efficiency of sampling within the region of interest. The percentage of points of interest achieves a value that is four times higher than when employing only GPR only. But, as can be seen in the 2D-diagrams of Figure 3, the GPR+I methodology is exploiting the region of interest by sampling points that are very close to each other. The clustering effect observed with GPR only is still present, although some of the clusters are clearly spatially extended compared to GPR. In comparison to the standard LHS technique, GPR and GPR+I enable the acquisition of more points of interest in poorly endowed or even unpopulated zones, such as at the frontier points—specifically at the extreme border of the aluminum radius zone ( $3\text{ }\mu\text{m}$ ), the lowest richness, and in proximity to the Al/CuO stoichiometric mixtures ( $\phi = 1$ ). Noticeably, GPR+I extends the region of interest towards nanoscaled CuO ( $r_{\text{CuO}} < 1\text{ }\mu\text{m}$ ). Particularly, points of interest are also found at low richness where neither LHS benchmark, nor GPR enable finding them. While the GPR+I strategy discovers a greater number of points of interest and extends the overall spatial domain in which these points are located, the overall shape of the cloud is still altered. This is particularly notable in the projection of points of interest in the  $\phi/r_{\text{CuO}}$  plane where the benchmark distribution shows well-spread and homogeneous spreading of the points of interest.

Activating the incentive component  $C$  of the acquisition function, after sampling 700 points with GPR+I, seems to modestly enhance the algorithm's efficiency in terms of the spatial distribution of the collected points of interest (Figure 3, 2D diagrams corresponding to GPR+I versus GPR+I+C). However, the calculation of the Voronoi area (Table III) for the points of interest in the final 1500 sampled points, reveals that the additional coverage results in a decrease in the mean value of the Voronoi area. Additionally, when using GPR+I+C strategy, the minimum value decreases, while the maximum value exhibits a slight increase compared to GPR+I strategy. These variations indicate that the dispersion of the points is smaller for GPR+I+C resulting in a more uniform coverage of the region. It has to be noted that, while GPR+I shows saturation in sampling points of interest at approximately 30%, the activation of  $C$  component in the acquisition function significantly improves both the percentage and total number of points of interest. GPR+I+C strategy enables to



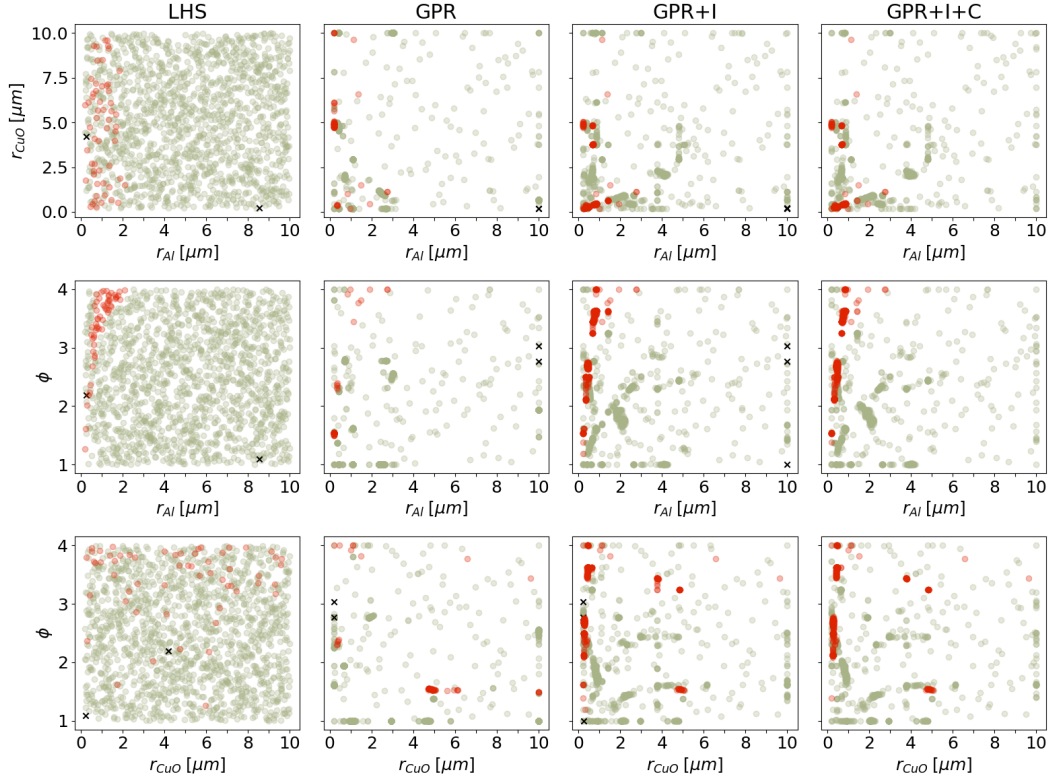


FIG. 3. Spatial distribution of the total number of sampled points (1500) projected onto main feature scale planes. Red balls corresponds to points of interest, while gray balls represent non-interesting points, and black crosses indicate outliers (out of the range).

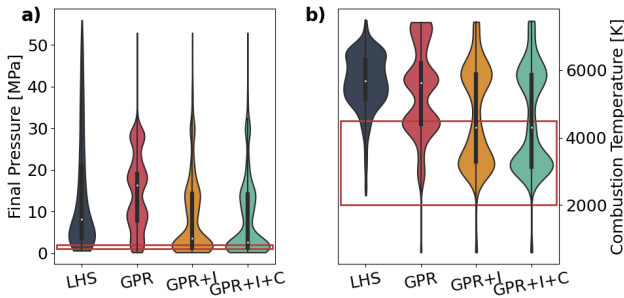


FIG. 4. Violin plots of the targets a) Final pressure, b) Combustion temperature obtained with LHS, GPR only and active sampling strategies. The red box shows the limits of the region of interest.

reach 40.3% (605 points out of 1500 total points) of points of interest in the final database, as opposed to 31.7% (476 points out of 1500 total points) when the exploration is guided with the "GPR+I" strategy. In comparison to the standard LHS technique, GPR+I+C provides an order of magnitude improvement in efficiency for identifying points of interest. The 605 points of interest sampled out of the total 1500 are close to the 653 found using the benchmark LHS, which required 19404 sampled points to be found. However, their spatial distribution is markedly different. The use of LHS enables the uniform sampling of points of interest within the

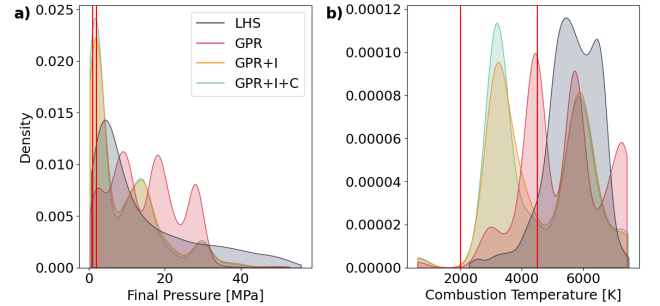


FIG. 5. KDE plots of the targets a) Final pressure, b) Combustion temperature obtained with LHS and active sampling strategies. The red lines mark the limits of the region of interest.

associated region of interest. The violin and Kernel Density Estimate (KDE) plots provide more detailed insights into the relationship between the created database and the targets, i.e., the final pressure and combustion temperature (Figure 4 and 5).

Analyzing the final pressure target, the violin plot generated with LHS (dark gray) reveals a unimodal distribution slightly above the region of interest, R1. This distribution appears compressed both below and above this specific region. In contrast, for the combustion temperature ( $T_{max}$ ), the distribution

TABLE III. Voronoi area after the complete simulation

Method	LHS	GPR	GPR+I	GPR+I+C
Mean	$1.9 \cdot 10^8$	$2.0 \cdot 10^8$	$1.5 \cdot 10^7$	$1.2 \cdot 10^7$
Min	$7.3 \cdot 10^4$	$1.6 \cdot 10^5$	$2.7 \cdot 10^1$	1.0
Max	$8.0 \cdot 10^9$	$1.2 \cdot 10^9$	$8.4 \cdot 10^8$	$8.9 \cdot 10^8$

is predominantly situated above the region of interest, with a narrow distribution located within that area. Guiding sampling with only GPR strategy (red), we observe a change in the distribution for both targets towards a more *distributed* shape. Although this results in an increase in samples within the region of interest for the combustion temperature, the same advantage is not evident for the final pressure,  $P_f$ . It's noteworthy that the uneven distribution aligns with the intrinsic nature of the GPR sampling approach. Upon applying the GPR+I strategy, the distribution of both targets undergo a significant change. The distribution of the final pressure becomes mostly concentrated within the region of interest, confirming the effectiveness of the exploration strategy, with the variation of the median (white dots) to almost inside the region of interest. A similar observation applies to the temperature distributions, where the GPR+I strategy leads to a split distribution, with more than half of the points now situated within the region of interest (and the median now inside the region of interest).

Finally, with the addition of C part, both median values are inside the region of interest, shifting from consistently outside the region of interest in other methods to being entirely within for the combustion temperature, and nearly on the edge for the final pressure. This indicates a transformation in the distribution shape towards the expected outcome. This behavior can be observed into more detail in Figure 5, where the region of interest is delineated by red vertical lines. The augmentation of the population density in the interest region using the GPR+I+C strategy is compared with GPR+I is clearly visible, which was more difficult to appreciate from the violin plots.

#### B. Region 2 guided exploration: discovering new Al/CuO thermite materials for high pressure generation

Herein, we will evaluate the efficiency of our algorithm in guiding the sampling towards the discovery of new thermites of interest spread in different region of the design space.

**Claudia :** Here I would only put equivalent of Fig 3 for R2 as well as violin plots and KDE plots + Equivalent Table III (Voronoi).

## IV. CONCLUSION

## V. REFERENCES

- <sup>1</sup>J. J. de Pablo, B. Jones, L. K. Cora, V. Ozolins, and A. P. Ramirez, "The materials genome initiative, the interplay of experiment, theory and computation," *Current Opinion in Solid State and Materials Science* **18**, 99–117 (2014).
- <sup>2</sup>K. Butler, D. Davies, H. Cartwright, O. Isayev, and A. Walsh, "Machine learning for molecular and materials science," *Nature* **559**, 547–555 (2018).
- <sup>3</sup>A. de Almeida, R. Moreira, and T. Rodrigues, "Synthetic organic chemistry driven by artificial intelligence," *Nature Reviews Chemistry* **3**, 589–604 (2019).
- <sup>4</sup>N. Brown, P. Ertl, R. Lewis, T. Luksch, D. Reker, and N. Schneider, "Artificial intelligence in chemistry and drug design," *Journal of Computer-Aided Molecular Design* **34**, 709–715 (2020).
- <sup>5</sup>A. O. Oliynyk, E. Antono, T. D. Sparks, L. Ghadbeigi, M. W. Gaultois, B. Meredig, and A. Mar, "High-throughput machine-learning-driven synthesis of full-heusler compounds," *Chemistry of Materials* **28**, 7324–7331 (2016).
- <sup>6</sup>T. Ueno, T. D. Rhone, Z. Hou, T. Mizoguchi, and K. Tsuda, "Combo: An efficient bayesian optimization library for materials science," *Materials Discovery* **4**, 18–21 (2016).
- <sup>7</sup>R. Ouyang, E. Ahmetcik, C. Carbogno, M. Scheffler, and L. M. Ghiringhelli, "Simultaneous learning of several materials properties from incomplete databases with multi-task siso," *Journal of Physics: Materials* **2**, 024002 (2019).
- <sup>8</sup>G. Pilania, J. E. Gubernatis, and T. Lookman, "Structure classification and melting temperature prediction in octet ab solids via machine learning," *Physical Review B* **91**, 214302 (2015).
- <sup>9</sup>P. C. Jennings, S. Lysgaard, J. S. Hummelshøj, T. Vegge, and T. Bligaard, "Genetic algorithms for computational materials discovery accelerated by machine learning," *npj Computational Materials* **5**, 46 (2019).
- <sup>10</sup>H. Matter, "Selecting optimally diverse compounds from structure databases : A validation study of two-dimensional and three-dimensional molecular descriptors," *Journal of Medicinal Chemistry* **40**, 1219–1229 (1997).
- <sup>11</sup>P. R. Wiecha, "Deep learning for nano-photonics materials – the solution to everything!?" *Current Opinion in Solid State and Materials Science* **28**, 101129 (2024).
- <sup>12</sup>V. Sanders, B. Asay, T. Foley, B. Tappan, A. Pacheco, and S. S.F., "Reaction propagation of four nanoscale energetic composites (al/moo3, al/wo3, al/cuo, and bi2o3)," *Journal of Propulsion and Power* **23**, 707–714 (2007).
- <sup>13</sup>P. Gandhi, M. Schoenitz, and E. Dreizin, "Evaluation and design of metal-based gas-generating energetic materials," *Combustion and Flame* **249**, 112615 (2023).
- <sup>14</sup>T. Wu, F. Sevely, B. Julien, F. Sodre, J. Cure, C. Tenailleau, A. Esteve, and C. Rossi, "New coordination complexes-based gas-generating energetic composites," *Combustion and Flame* **219**, 478–487 (2020).
- <sup>15</sup>Y. Aly, M. Schoenitz, and E. Dreizin, "Aluminum-metal reactive composites," *Combustion Science and Technology* **183**, 1107–1132 (2011).
- <sup>16</sup>H. Wang, B. Julien, D. J. Kline, Z. Alibay, M. C. Rehwoldt, C. Rossi, and M. R. Zachariah, "Probing the reaction zone of nanolaminates at s time and m spatial resolution," *The Journal of Physical Chemistry C* **124**, 13679–13687 (2020).
- <sup>17</sup>M. Zachariah, "Nanoenergetics: Hype, reality and future," *Propellants, Explosives, Pyrotechnics* **38**, 7 (2013).
- <sup>18</sup>V. Baijot, D.-R. Mehdi, C. Rossi, and A. Estève, "A multi-phase microkinetic model for simulating aluminum based thermite reactions," *Combustion and Flame* **180** (2017), 10.1016/j.combustflame.2017.02.031.
- <sup>19</sup>J. M. Epps, J.-P. Hickey, and J. Z. Wen, "Modelling reaction propagation for Al/CuO nanothermite pellet combustion," *Combustion and Flame* **229**, 111374 (2021).
- <sup>20</sup>E. Tichtchenko, B. Bedat, O. Simonin, L. Glavier, D. Gauchard, A. Esteve, and C. Rossi, "Comprehending the influence of the particle size and stoichiometry on al/cuo thermite combustion in close bomb: A theoretical study," *Propellants, Explosives, Pyrotechnics* **48**, e202200334 (2023).
- <sup>21</sup>K. M. De Souza and M. J. de Lemos, "Advanced one-dimensional modeling of thermite reaction for thermal plug and abandonment of oil wells," *International Journal of Heat and Mass Transfer* **205**, 123913 (2023).
- <sup>22</sup>M. M. Islam and A. Strachan, "Role of dynamical compressive and shear loading on hotspot criticality in RDX via reactive molecular dynamics," *Journal of Applied Physics* **128**, 065101 (2020).
- <sup>23</sup>E. Tichtchenko, A. Estève, and C. Rossi, "Modeling the self-propagation reaction in heterogeneous and dense media: Application to Al/CuO thermite," *Combustion and Flame* **228**, 173–183 (2021).
- <sup>24</sup>P. V. Balachandran, D. Xue, J. Theiler, J. Hogden, and T. Lookman, "Adaptive strategies for materials design using uncertainties," *Scientific Reports*



TABLE IV. Minimum and maximum values of  $\theta_k(u)$  as a function of the initial sample size,  $m$ 

Size	20	30	40	50	60	70	80	90	100
<i>in #</i>	1	1	0	3	4	0	3	3	4
<i>Min</i>	0.004	0.002	0.02	0.007	0.01	0.001	0.002	0.003	0.001
<i>Max</i>	0.10	0.13	0.15	0.12	0.11	0.14	0.11	0.11	0.1

- 6, 19660 (2016).
- <sup>25</sup>C. C. S. Freitas, F. C. Peixoto, and A. S. Vianna, "Simulation of a thermal battery using phoenix®," *Journal of Power Sources* **179**, 424–429 (2008).
- <sup>26</sup>H. Habu, M. Okada, M. Lto, K. Nozoe, T. Kawano, S. Matsumoto, and Y. Yoshida, "Thermite as a chemical heat source for the science payload," *Science and Technology of Energetic Materials* **73**, 147–152 (2012).
- <sup>27</sup>N. Banerjee, Y. Xie, M. Rahman, H. Kim, and C. H. Mastrangelo, "From chips to dust: The mems shatter secure chip," in *2014 IEEE 27th International Conference on Micro Electro Mechanical Systems (MEMS)* (2014) pp. 1123–1126.
- <sup>28</sup>F. Sevely, T. Wu, F. Sodre Ferreira, L. Segulier, V. Brossa, S. Charlot, A. Esteve, and C. Rossi, "Developing a highly responsive miniaturized security device based on a printed copper ammine energetic composite," *Sensors and Actuators A: Physical* **346**, 113838 (2022).
- <sup>29</sup>T. Wu and M. R. Zachariah, "Silver ferrite: a superior oxidizer for thermite-driven biocidal nanoenergetic materials," *RSC Adv.* **9**, 1831–1840 (2019).
- <sup>30</sup>T. Wu, B. Julien, H. Wang, S. Pelloquin, A. Esteve, M. R. Zachariah, and C. Rossi, "Engineered porosity-induced burn rate enhancement in dense al/kuo nanothermites," *ACS Applied Energy Materials* **5**, 3189–3198 (2022).
- <sup>31</sup>V. L. Deringer, A. P. Bartók, N. Bernstein, D. M. Wilkins, M. Ceriotti, and G. Csányi, "Gaussian process regression for materials and molecules," *Chemical Reviews* **121**, 10073–10141 (2021).
- <sup>32</sup>P. Virtanen, R. Gommers, T. E. Oliphant, M. Haberland, T. Reddy, D. Cournapeau, E. Burovski, P. Peterson, W. Weckesser, J. Bright, S. J. van der Walt, M. Brett, J. Wilson, K. J. Millman, N. Mayorov, A. R. J. Nelson, E. Jones, R. Kern, E. Larson, C. J. Carey, Í. Polat, Y. Feng, E. W. Moore, J. VanderPlas, D. Laxalde, J. Perktold, R. Cimrman, I. Henriksen, E. A. Quintero, C. R. Harris, A. M. Archibald, A. H. Ribeiro, F. Pedregosa, P. van Mulbregt, and SciPy 1.0 Contributors, "SciPy 1.0: Fundamental Algorithms for Scientific Computing in Python," *Nature Methods* **17**, 261–272 (2020).
- <sup>33</sup>H. Wang, B. van Stein, M. Emmerich, and T. Back, "A new acquisition function for bayesian optimization based on the moment-generating function," in *2017 IEEE International Conference on Systems, Man, and Cybernetics (SMC)* (2017) pp. 507–512.
- <sup>34</sup>G. P. Kontoudis and M. Otte, "Adaptive exploration-exploitation active learning of gaussian processes," in *2023 IEEE/RSJ International Conference on Intelligent Robots and Systems (IROS)* (2023) pp. 9448–9455.

## Appendix A: Initial sample size

We make our decision based on determining the minimum initial sample size,  $m$ , that satisfies the following criteria:

1. The dataset should include significant points of interest.
2. There must be a notable difference of two orders of magnitude between the minimum and maximum values of  $\theta_k$  within the acquired surrogate.
3. The minimum and maximum values of  $\theta_k$  should exhibit a strong correlation with the shape of  $E(\sigma_{\theta_k}(u))$ , as illustrated in Figure 6.

We set  $m$  equal to 100, as this choice ensures that the variance in the range of  $\theta_k$  results in an approximate 50% decrease

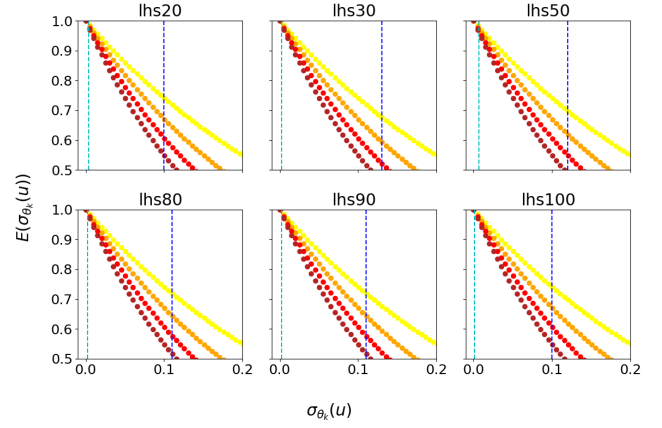


FIG. 6. Claudia? Only values that fulfill criteria 1 and 2...COMPLETE!.

TABLE V. Mean Standard Error for targets with surrogate model

Added points	GPR		GPR+I		GPR+I+C	
	$P_f$ [MPa]	$T_{max}$ [K]	$P_f$ [MPa]	$T_{max}$ [K]	$P_f$ [MPa]	$T_{max}$ [K]
200	3.74	3.5e+05	3.74	3.5e+05	3.74	3.5e+05
300	1.99	1.9e+05	7.6e-01	2.7e+02	7.6e-01	2.7e+02
400	1.99	1.4e+05	2.7e-01	1.1e+05	2.7e-01	1.1e+05
500	1.51	1.0e+05	4.1e-01	6.5e+04	4.1e-01	6.5e+04
600	1.22	8.3e+04	3.9e-01	5.4e+04	3.9e-01	5.4e+04
700	1.66	7.2e+04	4.8e-01	4.8e+04	4.8e-01	4.8e+04
800	1.43	6.2e+04	1.93	7.7e+04	3.1e-09	8.1e-01
900	1.25	5.4e+04	4.19	8.4e+04	1.1e-02	1.8e+04
1000	1.11	4.8e+04	5.77	7.7e+04	1.1e-01	9.5e+03
1100	1.00	4.3e+04	5.36	7.1e+04	8.8e-02	6.8e+03
1200	9.4e-01	4.3e+04	5.26	6.8e+04	8.9e-02	6.1e+03
1300	9.4e-01	4.1e+04	4.75	6.8e+04	9.5e-02	5.2e+03
1400	9.0e-01	3.8e+04	4.36	6.6e+04	1.79	4.1e+04
1500	8.5e-01	3.6e+04	4.02	6.1e+04	3.82	5.2e+04

in  $E(\sigma_{\theta_k}(u))$ . This facilitates a rapid adjustment of the function at the initial stages of the method.

## Appendix B: GPR

### 1. Parameter $a$

Plot on variation of STD on initial sample 6

### 2. Standard Deviation of Surrogate

Table V of MSE for targets for each method...

## Appendix C: R2

Tableau equivalent à TABLE II for R2